Civil, Architectural and Environmental Engineering Faculty Research & Creative Works

Civil, Architectural and Environmental Engineering

05 Feb 2024

Wearable MXene-Graphene Sensing Of Influenza And SARS-CoV-2 Virus In Air And Breath: From Lab To Clinic

Yanxiao Li

Zhekun Peng

Jiaoli Li

Congjie Wei

et. al. For a complete list of authors, see https://scholarsmine.mst.edu/civarc_enveng_facwork/2719

Recommended Citation

Wearable MXene-Graphene Sensing of Influenza and SARS-CoV-2 Virus in Air and Breath: From Lab to Clinic

Yanxiao Li, Zhekun Peng, Jiaoli Li, Congjie Wei, Shangbin Liu, Weixing Hao, Huanyu Cheng, Casey Burton, Yang Wang, Yue-Wern Huang, Chang-Soo Kim, Fang Yao Stephen Hou, DongHyun Kim, and Chenglin Wu*

The rapidly expanding severe acute respiratory syndrome coronavirus 2 (SARS-CoV-2) and its variants demand a continuous monitoring method through portable and wearable devices. Utilizing the rich surface chemistry and high chemical-to-electrical signal conversion of 2D MXene-graphene heterostructure thin films, a field-effect-transistor (FET) sensor, which has a flexible substrate to be assembled onto the mask and combines with a Bluetooth system for wireless transmission is developed, to detect the influenza and SARS-CoV-2 viruses in air and breath. At first, the developed sensors are examined in the laboratory through direct contact with sensing targets in solution form. The results show a low limit of detection (LOD) of 1 fg mL^{-1} for recombinant SARS-CoV-2 spike protein and 125 copies mL^{-1} for inactivated influenza A (H1N1) virus with high specificity in differing recombinant SARS-CoV-2 spike protein and inactivated H1N1 virus. Then the sensors are tested under various simulated human breathing modes through controlled exposure to atomizer-generated aerosols in an enclosed chamber and mask coverage. The results show the high sensitivity of the developed sensors under varying distances to the source, viral load, flow rate, and enclosed conditions. At last, clinical tests are carried out to demonstrate the robustness and potential field applications of the sensors.

1. Introduction

The total confirmed cases of SARS-CoV-2 have passed 700 million globally by April 2023. More and more contagious variants like Omicron have also emerged.[1] Access to personal protective equipment (PPE) for the health workforce has been identified as the key factor in strengthening the international health system's response to SARS-CoV-2.[2] Studies have shown that early SARS-CoV-2 patients emit a significant amount of SARS-CoV-2 viral particles through breathing, coughing, talking, or sneezing.[3] The use of medical/surgical face masks and filtering facepiece respirators (i.e., N95 or FFP2 or FFP3) has been recommended in conjunction with other mitigating methods to prevent transmission of respiratory pathogens.[4] Hence, a flexible and portable SARS-CoV-2 sensor that can be integrated with PPE is highly desirable.

Y. Li, J. Li, C. Wei, W. Hao, Y. Wang, C. Wu
Department of Civil
Architectural, and Environmental Engineering
Missouri University of Science and Technology
1401 N Pine St, Rolla, MO 65409, USA
E-mail: chenglinwu@tamu.edu

Y. Li
NETL Support Contractor
626 Cochran Mill Road, Pittsburgh, PA 15236, USA

Z. Peng, C.-S. Kim, D. Kim
Department of Electrical and Computer Engineering
Missouri University of Science and Technology
301 St Patrick's Ln, Rolla, MO 65409, USA

S. Liu, H. Cheng
Department of Material Science and Engineering
The Pennsylvania State University
221 Steidle Building, University Park, PA 16802, USA

W. Hao, Y. Wang
Department of Chemical
Environmental, and Materials Engineering
University of Miami
1251 Memorial Drive, Coral Gables, FL 33124, USA

H. Cheng
Department of Engineering Science and Mechanics
The Pennsylvania State University
212 Earth and Engineering Sciences Building, University Park, PA 16802, USA

C. Burton
Department of Chemistry
Missouri University of Science and Technology
400 W 11th St, Rolla, MO 65409, USA

C. Burton
Phelps Health
1000 W 10th Street, Rolla, MO 65401, USA

Y.-W. Huang
Department of Biological Sciences
Missouri University of Science and Technology
400 W 11th St, Rolla, MO 65409, USA

**ADVANCED
SCIENCE NEWS**

www.advancedsciencenews.com

**ADVANCED
MATERIALS
TECHNOLOGIES**

www.advmattechnol.de

Among different biosensing platforms and mechanisms,[5] the FET-based, electrochemical sensing method is one of the popular options for rapid and high-sensitivity sensing. Taking advantage of the surface effect and fast chemical-to-electrical signal conversion, only a small amount of sensing target is needed, which makes the FET biosensors more appealing for aerosol sensing. Regarding sensing materials, 2D materials are widely used for FET by researchers[6] due to their high flexibility, surface activity, excellent mechanical, and electrical properties.[7] Specially, the chemical vapor deposition (CVD) synthesized graphene is well-suited for FET sensor integration due to its large surface areas (wafer-scale[8]) and surface functionalization possibilities. However, graphene has high electron mobility (1.3×10^5 to 6×10^5 cm^2 V^{-1} s^{-1})[9] but no bandgap,[10] which introduces low on/off current ratio and limits the sensing sensitivity of the graphene-based FET sensor.[6a] As an alternative, we turn to MXenes, a new family of 2D metal carbides, which are synthesized by the selective etching of the "A" layers from the layered carbides known as MAX phases. Due to the chemical etching approach, MXenes have rich terminal groups (-O-, -OH, -F), which results in multilayer MXenes with band gaps and a semiconductor-like behavior.[11] Until now, various MXene nanosheet-based electrochemical biosensors have been investigated.[12] Among them, we selected Ti_2CT_x MXene, which is reported to obtain band gap of 0.91 eV and electron mobility ranging from 2.54×10^2 to 6.11×10^2 cm^2 V^{-1} s^{-1}.[13] It is reported that 2D material van der Waals (vdW) heterostructures allow adjusting the interfacial phenomenon for the tailored design of the sensing mechanism.[14] In our case, MXene-graphene heterostructure thin film provides improved band gap compared with pure graphene and improved electron mobility compared with pure MXene, which are suggested by numerous literatures for high-efficiency FET sensing.[10,15] Moreover, MXenes are flakes in micro scale and need continuous graphene as the substrate. Therefore, an MXene-graphene heterostructure thin-film-based FET biosensor is proposed.

In this paper, we developed a MXene-graphene-based FET mask sensor for SARS-CoV-2 and influenza virus detection. The mask sensor collects the sample through a microporous sponge (microporous silica aerogel with an average 100 ϵm pore size) on the top of MXene-graphene composite and transmits the signal

to a smartphone through a portable Bluetooth transmission unit (**Figure 1a**). The developed sensors were first tested by directly contacting with solutions of recombinant SARS-CoV-2 spike protein or inactivated influenza (H1N1) virus. Following, the sensors were tested by being exposed to aerosol with varying distances to source, viral load, flow rate, as well as enclosure conditions. The aerosols were generated by atomizers in both enclosed chambers and masks to simulate various human breathing modes. At last, the mask sensor was verified using clinical samples and patients' breath.

The lab test results showed that LOD was 1 fg mL^{-1} for recombinant SARS-CoV-2 spike protein and 125 copies mL^{-1} for inactivated influenza A (H1N1) virus. The sensing response time was 30 ms when the sensor and the sensing target were in direct contact, which was much lower than that for aerosol experiments (from 10 to 200 s) and patient breath tests (from 1 to 5 min). A closed environment in aerosol experiments introduced much higher sample collection efficiency. Moreover, the sensor was verified to be sensing specific and sensitive to concentration changes of the sensing target. Clinical test results showed that the developed sensors have high fidelity against rapid antigen tests. The patient breathing test by patient also demonstrates the real-time sensing capability of the developed sensor. Overall, the proposed MXene-graphene material-based on-mask sensing platform offers such a solution with robust, real-time sensing, fast response, high sensitivity, and portable features. It has a great potential for applications in the detection of different respiratory viruses.

2. Results and Discussion

2.1. Sensor Fabrication

The procedure for MXene-graphene FET mask sensor fabrication is shown in Figure 1b. At first, laser-induced graphene (LIG), which worked as drain and source electrodes, was made. The computer-designed serpentine layout on polyimide (PI) film was rapidly formed using a highly precise CO_2 laser system in an ambient environment. There was still some remaining PI underneath the LIG to ensure the mechanical integrity. This fabrication method is faster, easier to control and has lower cost compared with other flexible FET electrode fabrication methods in ref. [16] in which metals were used as electrodes. Then the Ag ink was dropped cast on LIG to reduce the resistance. For the FET device, the field effect mobility ϵ could be determined by,[17]

$$\mu = \frac{dI_{DS}}{dV_G} \times \frac{L}{WC_T V_{DS}} \tag{1}$$

Where L and W are the channel length and width, respectively, and C_T is the total capacitance per unit area. Therefore, when channel length and width ratio is higher, the field effect mobility of the FET device is larger. In our design, the length for both source and drain electrodes is 60 mm and the distance between them is 5 mm.

The MXene-graphene sensing material was synthesized and developed in the following sequence. The CVD grown, large-area, monolayer graphene was first transferred onto the PI film and covered the LIG region. Then the graphene surface was treated with UV light, followed by being deposited with Ti_2CT_x MXene

F. Y. S. Hou
Department of Biomedical Sciences &Health Care Administration
University of Wisconsin-Milwaukee
2400 E Hartford Ave, Milwaukee, WI 53211, USA
C. Wu
Department of Materials Science and Engineering
Missouri University of Science and Technology
1400 N Bishop, Rolla, MO 65409, USA
C. Wu
Department of Chemical and Biochemical Engineering
Missouri University of Science and Technology
1101 N State Street, Rolla, MO 65409, USA
C. Wu
Department of Civil and Environmental Engineering
Texas A&M University
201 Dwight Look Engineering Building, College Station, TX 77843-3136,
USA

**ADVANCED
SCIENCE NEWS**

www.advancedsciencenews.com

**ADVANCED
MATERIALS
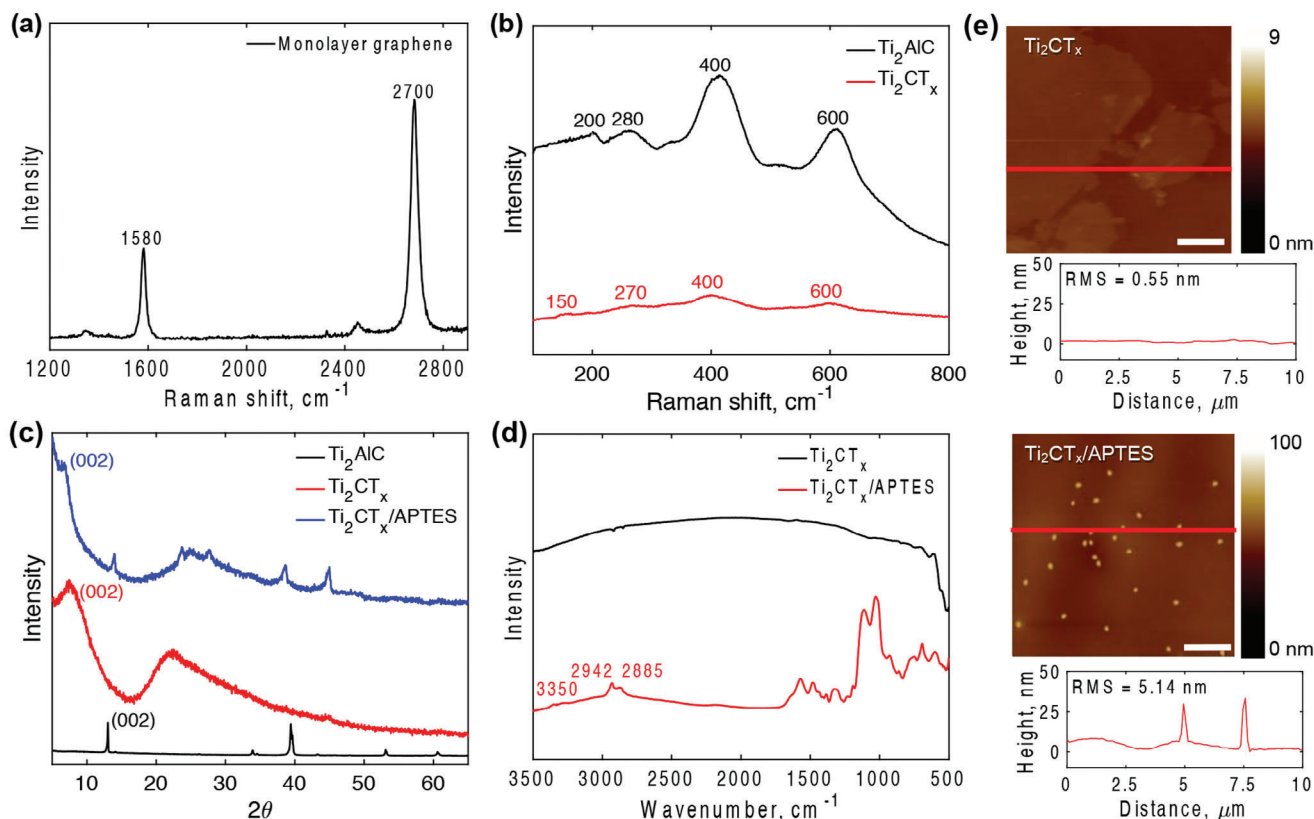TECHNOLOGIES**

www.advmattechnol.de
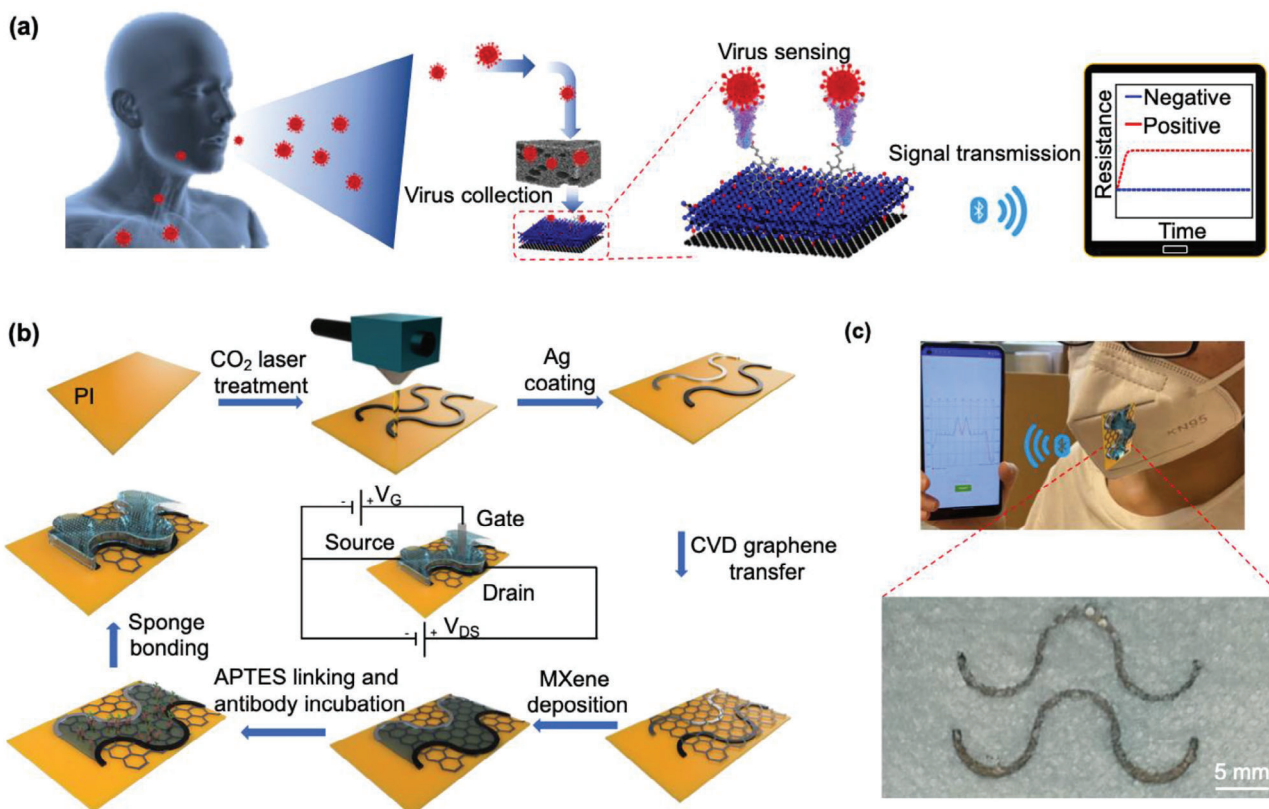
Figure 1. a) Illustration for the sensing procedure, b) procedures for MXene-graphene FET sensor fabrication, c) photo for real MXene-graphene FET mask sensor with zoom-in photo for electrodes.

colloidal solution to achieve covalent bonding between graphene and MXene. After that, the surface of MXene was functionalized with (3-Aminopropyl) triethoxysilane (APTES), followed by immobilization of SARS-CoV-2 spike antibody or influenza A (H1N1) HA polyclonal antibody. The details were described in the Experimental Section. After that, a microporous sponge was bonded onto the top of MXene-graphene composite between drain and source electrodes to collect spike protein or virus. The FET sensing circuit was also shown in Figure 1b, in which an Ag/AgCl electrode was used as the gate electrode. The gate electrode was totally immersed inside the electrolyte. After transferring the PI film onto a soft polydimethylsiloxane (PDMS) substrate, the MXene-graphene FET sensor was assembled onto a mask as shown in Figure 1c. SEM and AFM images for Ti_2CT_x MXene flakes on graphene are shown in Figure S1 (Supporting Information). Graphene covered with a large area of MXene flakes was observed.

2.2. Material Characterizations

Raman spectra for graphene, Ti_2AlC MAX phase, and Ti_2CT_x MXene were shown in **Figure 2a,b**. Characteristic Raman peaks of monolayer graphene at 1580 cm^{-1} (G band) and 2700 cm^{-1} (2D band) with an intensity ratio of 0.5 ($I_G : I_{2D}$) indicate the monolayer graphene is in high quality and defect-free.[18] Raman peaks of the Ti_2AlC MAX phase near 150 and 270 cm^{-1}

originated from Al–Ti vibrations. These peaks disappeared in Raman peaks of Ti_2CT_x MXene, indicating the successful removal of Al elements after etching. Besides Raman peaks near 400 and 600 cm^{-1}, new peaks near 200 and 280 cm^{-1} were all from Ti–C vibrations. XRD patterns (Figure 2c) further confirmed the successful etching of Ti_2AlC MAX. Typically, the (002) peak shifted to a lower angle after etching, from 13.03 to 7.45○. In addition, the disappearance of the peak at 39○ for Ti_2CT_x MXene indicates that Al atoms have been completely etched away. The reasons for choosing APTES are as follows. As is known, MXene is easy to oxidize due to hydroxyl groups on the surface. It has been reported that the silylation reaction between hydroxyl groups of MXene and APTES could greatly improve MXene stability.[19] Meanwhile, amino terminal group of APTES makes it easy to bond with antibodies.[20] XRD, FTIR, and AFM images provided the evidence of successful functionalization of APTES. After being functionalized with APTES, the (002) peak of Ti_2CT_x MXene shifted towards a smaller angle in the XRD pattern (from 7.45 to 6.89°) as shown in Figure 2c. This is attributed to the intercalation effect of APTES. FTIR spectrum of APTES functionalized MXene showed several new vibration peaks in comparison with that of pure MXene (Figure 2d). New peaks at 2885 and 2942 cm^{-1} (the asymmetric and symmetric stretches of -CH$_2$ groups on the alkyl chain), and 3350 cm^{-1} (the stretching vibration mode of the free amine) are from APTES. The stretching band of Si-O-Ti falling in 880–1295 cm^{-1} indicates the covalent bonding between APTES and MXene. APTES was also observed from the AFM

**ADVANCED
SCIENCE NEWS**

www.advancedsciencenews.com

**ADVANCED
MATERIALS
TECHNOLOGIES**

www.advmattechnol.de

Figure 2. a) Raman spectrum of monolayer graphene, b) Raman spectra of Ti_2AlC and Ti_2CT_x, c) XRD for Ti_2AlC, Ti_2CT_x, and APTES functionalized Ti_2CT_x, d) FTIR for Ti_2CT_x and APTES functionalized Ti_2CT_x, and e) AFM images for Ti_2CT_x and APTES functionalized Ti_2CT_x. The scale bar is 500 nm.

images (bright spots in Figure 2e). After APTES functionalization, the surface roughness (RMS) of MXene increased from 0.55 to 5.14 nm.

2.3. Advantages of MXene-Graphene FET Sensing

The selection of MXene-graphene as the sensing material for electrochemical signal conversion is based on the FET sensing mechanism. Compared with graphene-based FET sensor, MXene-graphene-based FET sensor has higher theoretical sensitivity because MXene-graphene has a non-zero band gap and the bonding between the antibody and MXene-graphene surface is covalent bond, while graphene has zero band gap and the interaction between the antibody and graphene is $\pi-\pi$ stacking. The details can be found in Note S1 (Supporting Information).

2.4. Direct Contact between Sensor and Sensing Target

Electrical characterizations were performed on the MXene-graphene FET sensor during the fabrication procedure and the details can be found in Note S2 (Supporting Information). Then the MXene-graphene FET mask sensor was tested with a series of concentrations of recombinant SARS-CoV-2 spike protein or inactivated influenza A (H1N1) virus as shown in **Figure 3**a. Five sensors were tested for every concentration of recombinant
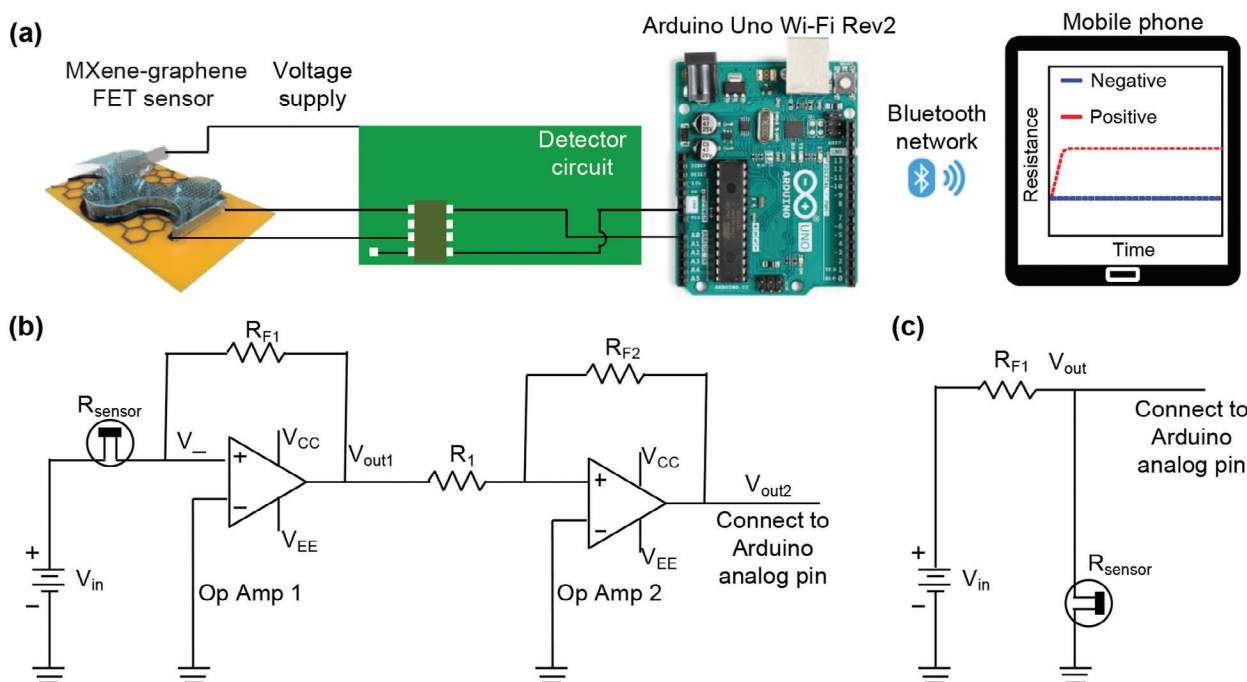
SARS-CoV-2 spike protein or inactivated influenza A (H1N1) virus. The sensing response time is 30 ms. I_{DS}–V_G curves (V_{DS} = 0.5 V) show that the LOD is 1 fg mL^{-1} for recombinant SARS-CoV-2 spike protein (Figure 3c) and 125 copies mL^{-1} for inactivated influenza A (H1N1) virus ((Figure 3e). The normalized right shifts of the Dirac point with the increasing concentrations of recombinant SARS-CoV-2 spike protein (from 1 fg mL^{-1} to 10 pg mL^{-1}) or inactivated influenza A (H1N1) virus (from 125 copies mL^{-1} to 250 000 copies mL^{-1}) were calculated by,

$$\frac{\Delta V}{V_0} = \frac{V - V_0}{V_0} \qquad (2)$$

Where V_0 is V_G value of the Dirac point when no spike protein or virus was applied, and V is V_G value of Dirac point when a certain concentration of spike protein or virus was applied. $\frac{\Delta V}{V_0}$ versus concentration curves with standard deviations were shown in Figure 3d,f. The normalized right shifts of the Dirac point increased with the increase of spike protein or virus concentration. The normalized signal changes range from 8.09% to 26.38% for recombinant SARS-CoV-2 spike protein, and from 7.22% to 22.22% for inactivated influenza A (H1N1) virus. The sensing specificity study in differing recombinant SARS-CoV-2 spike protein and inactivated H1N1 virus was also performed (Figure 3b). At first, the highest concentration of inactivated influenza A (H1N1) virus (250 000 copies mL^{-1}) and the lowest concentration of recombinant SARS-CoV-2 spike protein (1 fg mL^{-1})
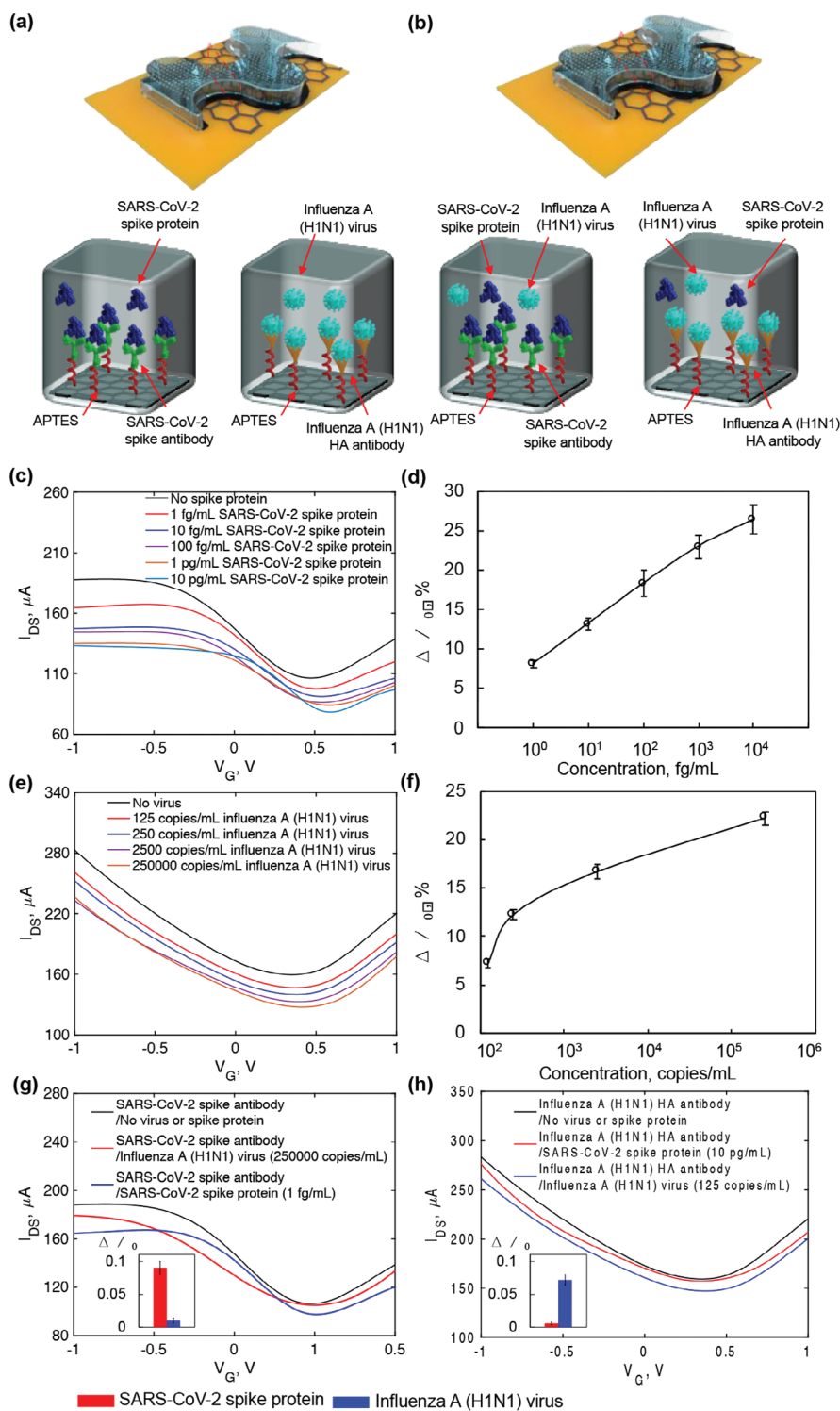
Figure 3. a) Illustration for SARS-CoV-2 spike antibody immobilized sensor for recombinant SARS-CoV-2 spike protein sensing and influenza A (H1N1) HA polyclonal antibody immobilized sensor for inactivated influenza A (H1N1) virus sensing, b) illustration for sensing specificity verification, c) IDS-VG curves (VDS = 0.5 V) for applying various concentrations of recombinant SARS-CoV-2 spike protein to SARS-CoV-2 spike antibody immobilized sensor, d) corresponding $\frac{\Delta V}{V_0}$ versus concentration curves, e) IDS-VG curves (VDS = 0.5 V) for applying various concentrations of inactivated influenza A (H1N1) virus to influenza A (H1N1) HA polyclonal antibody immobilized sensor, f) corresponding $\frac{\Delta V}{V_0}$ versus concentration curves (x axis is log plotted), g), h) IDS-VG curves (VDS = 0.5 V) for the sensing specificity study, with $\frac{\Delta V}{V_0}$ values in subset figures. The errors are standard deviations.

ADVANCED
SCIENCE NEWS
www.advancedsciencenews.com

ADVANCED
MATERIALS
TECHNOLOGIES
www.advmattechnol.de

Figure 4. a) Illustration for real-time resistance monitor system, b) auto-balancing bridge impedance measurement circuit, c) voltage divider resistance measurement circuit.

used in the previous experiment were applied to SARS-CoV-2 spike antibody immobilized sensor in sequence. The obtained I_{DS}–V_G curves (V_{DS} = 0.5 V) are shown in Figure 3g. Then the highest concentration of recombinant SARS-CoV-2 spike protein (10 pg mL^{-1}) and the lowest concentration of influenza A (H1N1) virus (125 copies mL^{-1}) used in the previous experiment were applied to influenza A (H1N1) HA polyclonal antibody immobilized sensor in sequence. The obtained I_{DS}–V_G curves (V_{DS} = 0.5 V) are shown in Figure 3h. The normalized right shifts of the Dirac point values were calculated using Equation (2) and shown in subset figures of Figure 3g,h. We observed that normalized right shift values when antibody and spike protein or virus are paired (7.26–9%) are significantly higher than those when antibody and spike protein or virus are not paired (0.6–1%). These results verified the high sensing specificity of our sensor to spike protein or virus in differing recombinant SARS-CoV-2 spike protein and inactivated H1N1 virus.

2.5. Sensing of Spike Protein or Virus in Atomizer Generated Aerosol

The MXene-graphene FET mask sensor was also verified for the function in collecting and sensing recombinant SARS-CoV-2 spike protein and inactivated influenza A (H1N1) virus inside the aerosol. Atomizer generated aerosol with spike protein or virus was sprayed to sensors through a rubber tube.
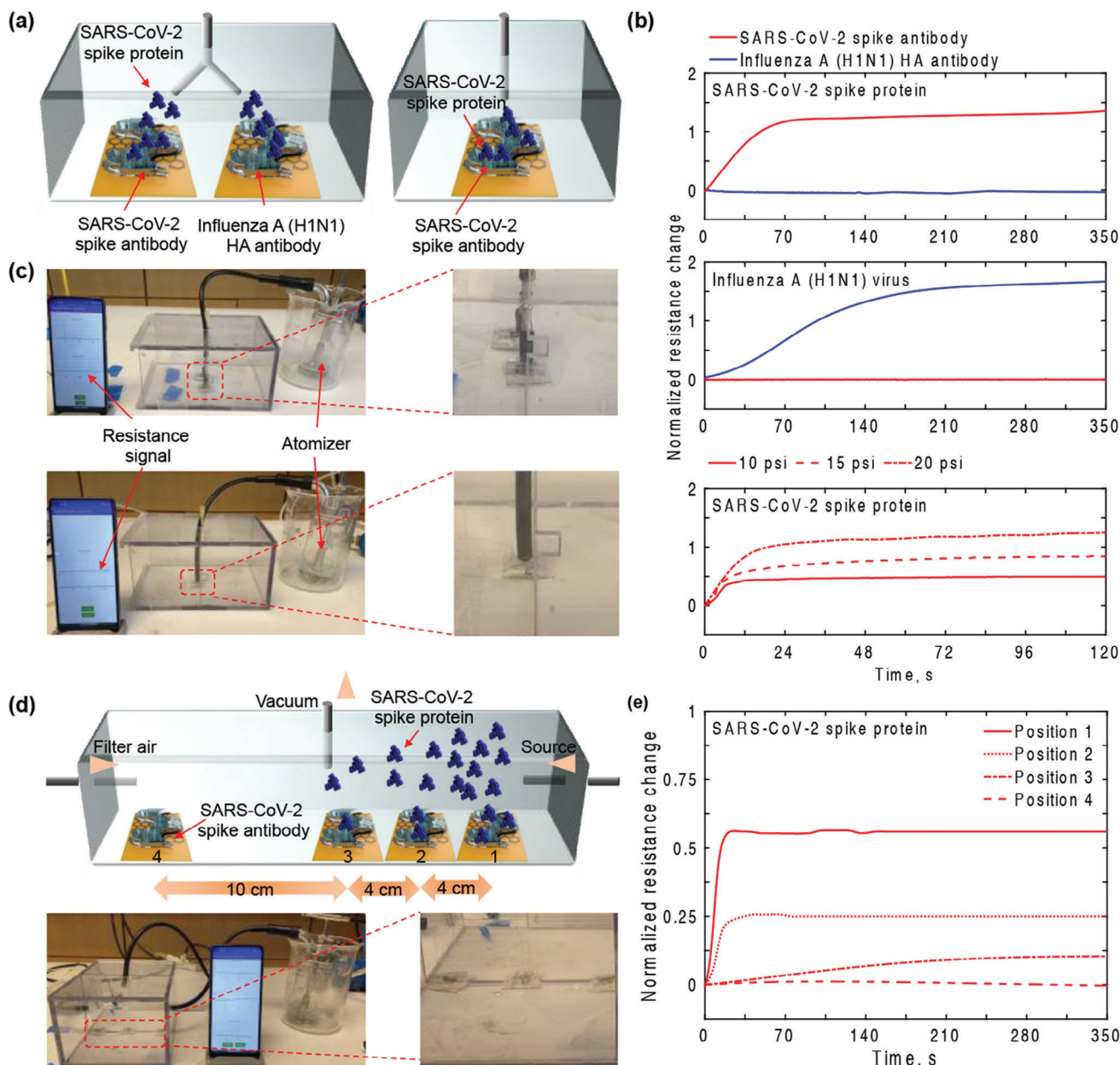
2.5.1. Bluetooth Circuit

The real-time resistance of the mask sensor was recorded and transmitted to a smartphone through a Bluetooth module. As

shown in **Figure 4a**, the detector circuit supplied the source and bias voltage to the sensor and measured the potential voltage difference at different nodes on the circuit. Arduino Uno Wi-fi Rev2 was connected to the output of the sensor and continuously sampled the potential voltage difference on the detector circuit using analog pins. Using an analytical equation to convert the measured voltage into the change in resistance, the result was transmitted from the Arduino to a smartphone through an in-house data acquisition and plotting application using Bluetooth network. Two detector circuits are suggested. Figure 4b demonstrates the auto-balancing bridge impedance measurement circuit. V_- of the operational amplifier (op amp) 1 served as virtual ground, where the potential voltage was equal to zero. Therefore, the current through R_{F1} was balanced with the current through R_{sensor}. The op amp 2 was used for inverting the output of the first op amp, which is negative, to positive so that the potential value could be read by Arduino analog pins. The measured resistance was calculated by the following analytical equation

$$R_{sensor} = \frac{V_{in}}{V_{out2}} \frac{R_{F1} R_{F2}}{R_1} \tag{3}$$

where V_{in} is the source voltage, V_{out2} is the potential measured at the output of op amp 2, R_{F1} and R_{F2} are the feedback resistors, and R_1 is the resistor at the inverting input of op amp 2. Op amp 1 must be a dual-supply amplifier in order to generate negative output. Figure 4c shows a relatively simpler measurement circuit compared with the previous one. V_{in} is the source voltage, R_1 is the resistor before R_{sensor}, and V_{out} is the potential voltage measured at the node between R_1 and R_{sensor}. R_1 and R_{sensor} were

**ADVANCED
SCIENCE NEWS**

www.advancedsciencenews.com

**ADVANCED
MATERIALS
TECHNOLOGIES**

www.advmattechnol.de

Figure 5. a) Illustrations for experimental setup of sensing specificity verification and flow rate effect study in aerosol experiments, b) corresponding normalized resistance change versus time curves, c) photos for experimental setup of sensing specificity verification and flow rate effect study in aerosol experiments, d) illustration and photo for experimental setup of viral load study in aerosol experiments, and e) corresponding normalized resistance change versus time curves.

used as voltage dividers to derive the resistance of R_{sensor}. The measured resistance was calculated by

$$R_{sensor} = \frac{V_{out}}{V_{in} - V_{out}} R_1 \qquad (4)$$

Both measurement circuits work for our system. Auto-balancing circuit requires more components, such as op amps and more resistors, but it provides more accurate results because the output impedance of the op amp is very low. On the other hand, voltage divider circuit is much simpler and convenient for miniaturiza-

tion of the whole system, but the accuracy cannot be guaranteed when R_{sensor} is high (above 100 kΩ). Therefore, the final decision on which circuit is to be applied depends on the resistance range of the immunosensor under the certain bias and the application target.

2.5.2. Sensing Specificity

Using the circuit mentioned above, sensing specificity of the sensor was verified at first using the experimental setup as shown in
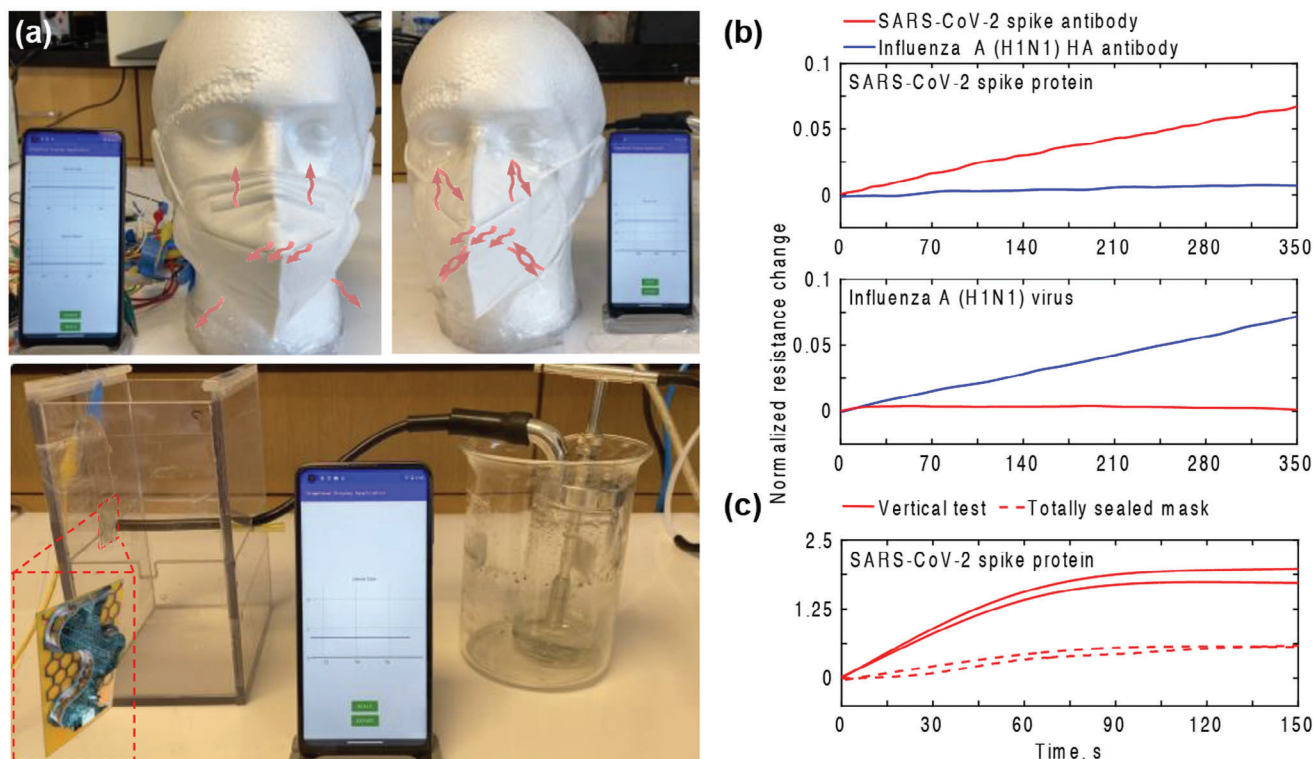
Figure 6. a) Experimental setup for partially sealed sensor (top left), totally sealed sensor (top right), and vertically placed sensor sensing in a closed chamber (bottom), b) normalized resistance change versus time curves for sensing specificity study, and c) normalized resistance change versus time curves for totally sealed sensor and vertically placed sensor.

Figure 5a (left) and c (top). Normalized resistance change was calculated by
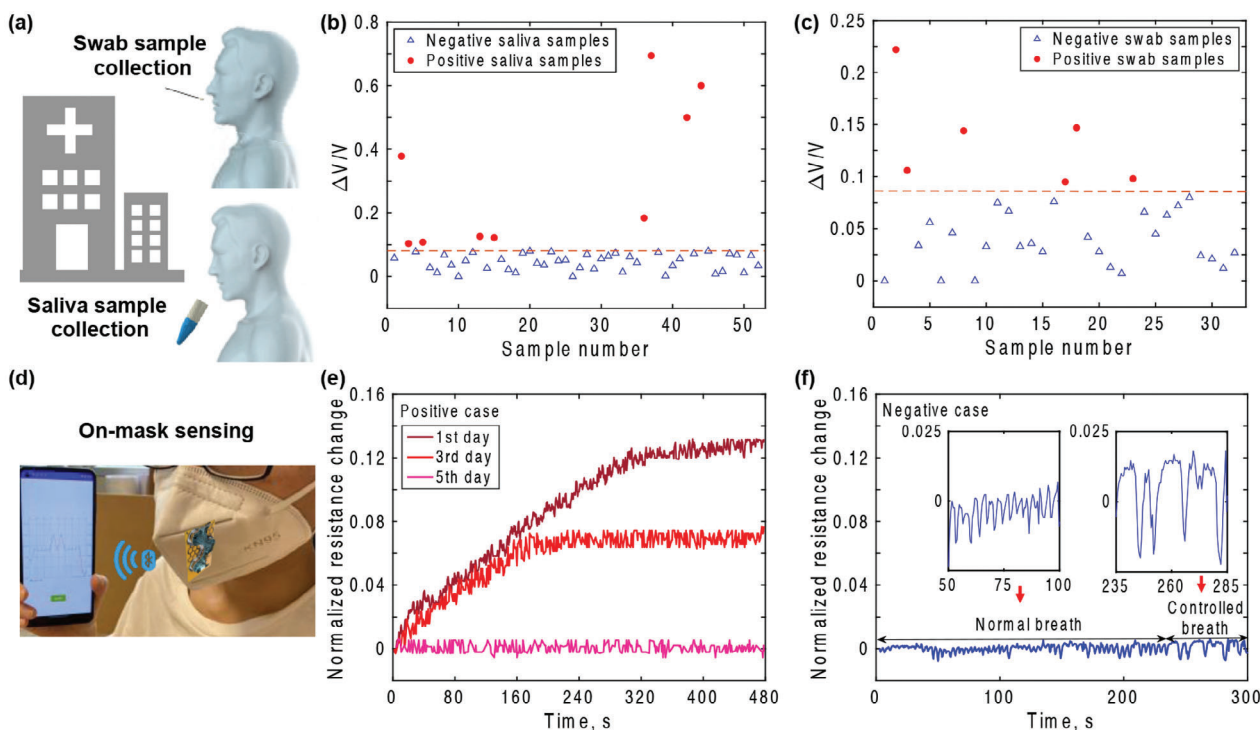
$$\frac{\Delta R}{R_0} = \frac{R - R_0}{R_0} \qquad (5)$$

Where R_0 is the resistance of the sensor when being sprayed with pure artificial saliva, and R is the real-time resistance of the sensor when being sprayed with spike protein or virus inside artificial saliva. Normalized resistance changes versus time curves in Figure 5b shows that significant normalized resistance changes were observed when the antibody is paired with its corresponding spike protein or virus. When spraying 5 fg mL^{-1} of recombinant SARS-CoV-2 spike protein onto both SARS-CoV-2 spike antibody immobilized sensor and influenza A (H1N1) HA polyclonal antibody immobilized sensor, the normalized resistance change for SARS-CoV-2 spike antibody immobilized sensor is much greater than that for influenza A (H1N1) HA polyclonal antibody immobilized sensor. Similarly, when spraying 250 000 copies mL^{-1} of inactivated influenza A (H1N1) virus onto both SARS-CoV-2 spike antibody immobilized sensor and influenza A (H1N1) HA polyclonal antibody immobilized sensor, the normalized resistance change for influenza A (H1N1) HA polyclonal antibody immobilized sensor is much larger than that for SARS-CoV-2 spike antibody immobilized sensor. It should be noted that when antibody and spike protein or virus are paired, the normalized resistance change increases quickly before reaching a plateau and staying stable. The time for reaching stable was ≈70 s for recombinant SARS-CoV-2 spike protein sensing and ≈210 s for inactivated influenza A (H1N1) virus sensing. This time includes both sample collection process and electrochemical sensing process.

2.5.3. Flow Rate Effect

Aerosol flow rates are different when people are breathing, coughing, talking, or sneezing. To investigate how our mask sensor will respond to these behaviors, recombinant SARS-CoV-2 spike protein (5 fg mL^{-1}) in artificial saliva with different flow rates was sprayed onto SARS-CoV-2 spike antibody immobilized sensors as shown in Figure 5a (right) and c (bottom). Flow rates were chosen as 8.75 × 10^{-3}, 1.31 × 10^{-2}, and 1.75 × 10^{-2} fg s^{-1}, which were generated by an atomizer under pressure of 10, 15, and 20 psi, respectively. Normalized resistance change versus time curves are shown in Figure 5b. The curves were linear before reaching the plateau and stayed stable after reaching the plateau. The plateau value is highest for flow rate of 1.75 × 10^{-2} fg s^{-1}, followed by 8.75 × 10^{-3} fg s^{-1} and 1.31 × 10^{-2} fg s^{-1}. This is because a higher flow rate generated a higher concentration of spike protein and introduced a larger amount of bonding between antibody and spike protein per area, which resulted in a larger normalized resistance change. In addition, the increasing speed of the normalized resistance change, which is reflected by the slope of the linear stage, is similar under various flow rates.

**ADVANCED
SCIENCE NEWS**

www.advancedsciencenews.com

**ADVANCED
MATERIALS
TECHNOLOGIES**

www.advmattechnol.de

Figure 7. a) Illustration for nasopharyngeal swab and saliva clinical sample collections, b) normalized right shift of the Dirac point for saliva samples, c) normalized right shift of the Dirac point for nasopharyngeal swab samples. Dash lines denote threshold for differing positive and negative cases. d) Photo for real-human on-mask sensing, and normalized resistance change versus time curves for e) positive case and f) negative case. Subsets are zoom in curves under normal breath and controlled breath.

2.5.4. Effect of Viral Load

Owing to the low LOD and fast response, our sensor has the potential to be placed in public buildings for real-time monitoring and locating areas with high viral load. To verify this, filtered air and aerosol with recombinant SARS-CoV-2 spike protein (5 fg mL^{-1}) in artificial saliva were input from two sides of a chamber, and a vacuum pump was placed from top of the chamber as shown in Figure 5d. Sensors were placed in positions 1, 2, 3, and 4 with a distance of 4 cm (between position 1 and 2, 2 and 3) or 10 cm (between position 3 and 4). Normalized resistance change versus time curves for these 4 sensors are shown in Figure 5e. The sensor in position 1 had the largest signal change among the 4 sensors. This is because position 1 was closest to the spike protein spraying tube and received the highest concentration of spike protein, followed by sensors in position 2 and 3. In contrast, there is almost no signal change for the sensor in position 4, which indicates that the concentration of spike protein in position 4 was lower than LOD. All results above show that the sensor detected and located various concentrations of virus in aerosol successfully.

2.5.5. Dummy Model Verification

To verify that the sensor is fully functional when being worn, the sensor was used to detect spike protein or virus in aerosol generated by the atomizer and sprayed through a tube inside the

mouth of a dummy model. At first, sensing specificity in differing recombinant SARS-CoV-2 spike protein and inactivated H1N1 virus was verified (**Figure 6a**, top right). As expected, normalized resistance changes versus time curves (Figure 6b) showed there was only significant single change when antibody and spike protein or virus were paired. However, the curves haven't reached the plateau even after 350 s. The reason was suspected to be that the face of the dummy model wasn't sealed well by the mask. Aerosol leaked through the unsealed area and thus introducing a small, normalized resistance change (≈7%) even when the spike protein or virus paired with the antibody. To verify this assumption, recombinant SARS-CoV-2 spike protein (5 fg mL^{-1}) in artificial saliva was applied to the SARS-CoV-2 spike antibody immobilized sensor within a totally sealed mask (Figure 6a, top right). The normalized resistance changes were much larger than those for partially sealed cases and reached plateau (≈62%) within 70 s (Figure 6c, dash lines). Moreover, when the aerosol was sprayed vertically onto the sensor inside a closed chamber (Figure 6a, bottom), the signal change was even larger (≈188%) (Figure 6c, solid lines). Multiple experiments showed consistency. These results suggest that a closed environment is critical for high sensing efficiency.

2.6. Clinical Sample Tests

First, 52 saliva samples and 32 nasopharyngeal swabs from SARS-CoV-2 patients and healthy subjects were collected and

**ADVANCED
SCIENCE NEWS**

www.advancedsciencenews.com

**ADVANCED
MATERIALS
TECHNOLOGIES**

www.advmattechnol.de

tested by directly contacting with sensors (**Figure** 7a, details are in Experimental Section). The normalized right shifts of the Dirac point for saliva samples and nasopharyngeal swab samples are shown in Figure 7b and Table S1 (Supporting Information), Figure 7c and Table S2 (Supporting Information), respectively. The threshold for positive cases was determined by normalized right shift of Dirac point at LOD (1 fg mL^{-1}), which is 0.081 ± 0.004 as shown in Figure 3d. Virus concentrations for positive cases were calculated according to the linear relationship between the normalized Dirac point shift and virus concentration (Figure 3d). The regression equation is expressed as $\frac{\Delta V}{V_0}$ = 0.046lgC + 0.085, in which C is the concentration for SARS-CoV-2 spike protein. And the correlation coefficient value (R^2) is 0.994. Then the obtained virus concentrations with fg mL^{-1} were converted to copies mL^{-1} using the molecular weight of recombinant SARS-CoV-2 spike protein S1 (76.5 kDa), which is provided by the vendor. After comparing the test results from our sensors with those from the rapid antigen test method (provided by the hospital), no false positive or false negative case was found. And the response time is 30 ms. These indicate that the sensor is fast-responded and very accurate in SARS-CoV-2 virus (inside nasopharyngeal swabs and saliva) sensing. Second, sensors were worn by volunteers to collect and sensing the breathing from humans. The output signal was collected by a Bluetooth circuit and transmitted to a smartphone (Figure 7d). For the positive case, the volunteer was tested three times (once for every two days) after SARS-CoV-2 infections. As shown in Figure 7e, the normalized resistance changes for the first and second tests increased at first, then reached the peak value (0.13 for the first test and 0.07 for the second test) after 320 and 180 s, respectively. The time includes the sample collection process and relates to whether the mask is fully sealed, which is also concluded from the previous section. Finally, normalized resistance changes values stayed stable. Almost no normalized resistance change was observed for the third test, which is similar to the curve in Figure 7f (from the negative case). This indicates that the volunteer turned to be negative after 5 days. The signal fluctuations in curves are very small (within 2%) and are related to the human's exhalation and inhalation as shown in the subset of Figure 7f. Different breathing modes have different fluctuation patterns. More results can be found in Figures S4 and S5 (Supporting Information). These assessment outcomes suggest that the sensor is very sensitive and fast-responded in the real scenario. When comparing sensing performance of our sensor with other graphene-based FET sensors in SARS-CoV-2 detection as shown in Table S3 (Supporting Information), our sensor shows advantages in flexibility, portability, fast response, and low LOD.

3. Conclusion

We developed a flexible and wireless FET mask sensor using MXene-graphene as the sensing material. When directly contact with sensing targets, sensors are found to be very sensitive for recombinant SARS-CoV-2 spike protein and inactivated influenza A (H1N1) virus detection. This high sensitivity was explained theoretically based on the non-zero band gap of MXene-graphene composite. The low LOD and fast response time were also observed, which are attributed to the covalent bonding between MX-

ene and APTES. The sensors were also verified with recombinant SARS-CoV-2 spike protein and inactivated influenza (H1N1) HA virus in aerosol generated by atomizer. Results show that sensors successfully collected the spike protein or virus inside the aerosol and the collection efficiency is related to whether the sensing environment is closed. In addition, the sensing signal is sensitive to the aerosol flow rate and viral load inside the aerosol, which indicates the potential application of our sensor in tracing viruses in public buildings. At last, saliva and nasopharyngeal swabs collected from SARS-CoV-2 patients and healthy subjects were applied to our sensors. Results agree well with rapid antigen test and virus concentration for positive cases are quantified. When hospital subjects wear our sensors for real-time monitoring, the sensing signal is observed to change with various virus concentrations and the noise-to-signal ratio is very low. Moreover, the noise is related to human breathing modes. Overall, the fabricated wireless and flexible mask sensor shows great potential of applications in rapidly and continuously monitoring and differentiating various kinds of respiratory viruses through breath or air. More sensing targets, like DNA, are planned to be tested using the platform in the future. The effective time and how to improve the effective time for the MXene-graphene FET sensor also need to be studied for real applications.

4. Experimental Section

Experimental Method: Raman spectra were acquired with a micro-Raman spectrometer (Horiba LabRAM ARAMIS) with 632.8 nm He–Ne laser, 50 × objective. AFM images were acquired by Digital Instruments Nanoscope IIIA under tapping mode using a 6 nm-diameter AFM tip with a 2 N m^{-1} cantilever. The X-ray diffraction (XRD, PANalytical, Phillips MPD) was acquired with Cu K $<\alpha>$ radiation (λ = 1.5406 Å) at U = 45 kV, I = 40 mA. Fourier-transform infrared spectroscopy (FT-IR) was acquired using Nicolet 4700 FT-IR.

Materials: Recombinant SARS-CoV-2 spike protein S1 (His Tag) with molecular mass of 76.5 kDa was purchased from SinoBiological (40591-V08H, Wayne, PA). SARS-CoV-2 spike antibody (Chimeric monoclonal antibody) was purchased from SinoBiological (40150-D001, Wayne, PA). The inactivated influenza A (H1N1) virus was purchased from Microbiologics (HE0029N, St. Cloud, MN). Influenza A (H1N1) HA polyclonal antibody was purchased from ThermoFisher Scientific (PA5-34929, Waltham, MA). Stabilized artificial saliva with pH of 7 was purchased from Pickering Laboratories (ASTM E2720-16, Mountain View, CA). Viral transport medium (VTM) was purchased from Innovative Research (Novi, MI). The Ti$_2$AlC MAX phase (325 mesh, particle size ≤ 45 µm) was purchased from Jinlin 11 Technology Co., Ltd.

Electrodes Fabrication: Ag ink-coated CO$_2$ LIG[21] was used as drain and source electrodes.

Graphene Synthesis and Transfer: Large-area monolayer graphene was grown by the CVD method[22] on a 2 × 10 cm copper foil. The copper foil with graphene on top was spin-coated with PMMA (20 mg mL^{-1} in chlorobenzene) under 4000 rpm for 30 s, followed by PMMA curing (180 °C for 3 min) and copper etched away (≈1 h). Then the remaining graphene/PMMA was cleaned with deionized (DI) water for several times, followed by transferred onto the PI substrate with electrodes. Finally, PMMA was removed by soaking in acetone solution.

MXene Synthesis and Transfer: Ti$_2$CT$_x$ MXene was synthesized by the selective etching method.[23] The etchant is prepared by dissolving 1.6 g LiF in 20 mL of 9 M HCl and magnetic stirring for 0.5 h. Then 1 g of Ti$_2$AlC MAX phase was slowly mixed into the etchant. The mix was stirred for 24 h at 35 °C, followed by repeated washing with DI water and centrifugation until the pH of supernatant reached 5.5–6.0. After 2 h sonication and 1 h centrifugation at 3500 rpm, the supernatant was taken out and freeze

**ADVANCED
SCIENCE NEWS**

www.advancedsciencenews.com

**ADVANCED
MATERIALS
TECHNOLOGIES**

www.advmattechnol.de

dried to prepare Ti_2CT_x powder. 5 mg mL^{-1} Ti_2CT_x aqueous colloidal solution was prepared by sonication of Ti_2CT_x powder in DI water. The ≈5 nm thick MXene flakes on graphene were prepared by drop casting 5 mg mL^{-1} Ti_2CT_x aqueous colloidal solution onto UV exposed graphene surface and drying in a vacuum.

Antibody Immobilization: A 50 µL APTES (volume ratio: 1:50 in DI water) was sprayed onto Ti_2CT_x surface and left for 4 h at room temperature. Then Ti_2CT_x MXene surface was rinsed several times with DI water to remove extra APTES. After that, the functionalized Ti_2CT_x surface was exposed to 10 µL of 250 µg mL^{-1} SARS-CoV-2 spike antibody or 10 µL of 10 µg mL^{-1} influenza A (H1N1) antibody, which were prepared in 1 × PBS (pH 7.4). After incubating for 4 h, extra antibody was removed by washing with 1 × PBS with 0.05% Tween 20 and DI water in sequence. Finally, Bovine Serum Albumin (BSA, 1 mg mL^{-1}) was incubated on Ti_2CT_x MXene surface for 2 h, and used as a blocking agent to prevent non-specific binding of the antigen onto Ti_2CT_x MXene surface. Extra BSA was removed by rinsing with 1 × PBS and DI water for several times.

FET Characterization: A Keithley 4200 semiconductor characterization system was used to apply gate and drain-source voltages and measure the drain-source current. Artificial saliva was used as an electrolyte to maintain an efficient gating effect.

Clinical Sample Preparation: Clinical samples used in this study were collected from subjects as part of registered protocols approved by the Institutional Review Board (IRB) of Phelps Health. All patients provided written informed consent (IRB registration number: PH-21-001-A2). Both saliva samples and nasopharyngeal swabs from SARS-CoV-2 patients or healthy subjects were collected. After collecting nasopharyngeal swab samples, the swab was diluted in 5 mL VTM. After saliva samples collection, 1 mL of saliva samples were taken out and mixed with 5 mL stabilized artificial saliva. After vortex shaking for 1 min, 50 µL of the prepared solution was used for FET sensing.

Aerosol Spray: The Collison Nebulizer (Waltham, MA, USA) was used to generate aerosols. The Collison Nebulizer achieves particle dispersion with a high-velocity air jet generated by high-pressure air passing through a nozzle. The air jet forms a low-pressure region that causes the spike protein or virus solution to rise in a feed tube and be nebulized into droplets. The nebulization occurs by the entrainment of the air jet into the solution through a cylindrical rod, which atomizes the solution into droplets. The distribution of droplet diameters is large. The large particles (>30 µm) collide with the vessel wall and return to the solution reservoir, while the smaller particles (0.25– 0 µm) exit through the outlet port with the airflow.

Supporting Information

Supporting Information is available from the Wiley Online Library or from the author.

Conflict of Interest

The authors declare no competing financial interest.

Author Contributions

Y.X.L synthesized graphene and MXene and performed material characterizations, sensor fabrications, and sensing measurements. Z.K.P designed and made the Bluetooth circuit, and developed a smartphone app. J.L.L. participated in the sensor fabrication. C.J.W and S.B.L drew the illustration figures. H.Y.C, C.B, Y.W, Y.W.H, C.K, F.Y.S.H, D.K, and C.L.W conceived and supervised the project, and designed experiments. All the authors wrote the manuscript, and reviewed, discussed, and approved the results and conclusions of the paper.

Data Availability Statement

The data that support the findings of this study are available on request from the corresponding author. The data are not publicly available due to privacy or ethical restrictions.

[1] S. S. A. Karim, Q. A. Karim, *Lancet* **2021**, *398*, 2126.

[2] W. H. Organization, World Health Organization. Regional Office for Europe **2020**.

[3] a) K. K. Coleman, D. J. W. Tay, K. S. Tan, S. W. X. Ong, M. H. Koh, Y. Q. Chin, H. Nasir, T. M. Mak, J. J. H. Chu, D. K. Milton, *medRxiv* **2021**; b) Z. Noorimotlagh, N. Jaafarzadeh, S. S. Martínez, S. A. Mirzaee, *Environ. Res.* **2021**, *193*, 110612; c) R. Dhand, J. Li, *Am. J. Respir. Crit. Care Med.* **2020**, *202*, 651.

[4] a) W. H. Organization, World Health Organization **2020**; b) E. N. Perencevich, D. J. Diekema, M. B. Edmond, *JAMA, J. Am. Med. Assoc.* **2020**, *323*, 2252.

[5] a) P. Q. Nguyen, L. R. Soenksen, N. M. Donghia, N. M. Angenent-Mari, H. De Puig, A. Huang, R. Lee, S. Slomovic, T. Galbersanini, G. Lansberry, H. M. Sallum, E. M. Zhao, J. B. Niemi, J. J. Collins, *Nat. Biotechnol.* **2021**, *39*, 1366; b) Q. Xue, X. Kan, Z. Pan, Z. Li, W. Pan, F. Zhou, X. Duan, *Biosens. Bioelectron.* **2021**, *186*, 113286; c) A. Raziq, A. Kidakova, R. Boroznjak, J. Reut, A. Öpik, V. Syritski, *Biosens. Bioelectron.* **2021**, *178*, 113029; d) L. Huang, L. Ding, J. Zhou, S. Chen, F. Chen, C. Zhao, J. Xu, W. Hu, J. Ji, H. Xu, G. L. Liu, *Biosens. Bioelectron.* **2021**, *171*, 112685; e) Y. Su, G. Chen, C. Chen, Q. Gong, G. Xie, M. Yao, H. Tai, Y. Jiang, J. Chen, *Adv. Mater.* **2021**, *33*, 2101262; f) B. Liu, A. Libanori, Y. Zhou, X. Xiao, G. Xie, X. Zhao, Y. Su, S Wang, Z. Yuan, Z. Duan, J. Liang, Y. Jiang, H. Tai, J. Chen, *ACS Appl. Mater. Interfaces* **2022**, *14*, 7301; g) C. Chen, M. Jiang, X. Luo, H. Tai, Y. Jiang, M. Yang, G. Xie, Y. Su, *Sens Actuators B Chem* **2022**, *370*, 132441; h) Y. Su, W. Li, L. Yuan, C. Chen, H. Pan, G. Xie, G. Conta, S. Ferrier, X. Zhao, G. Chen, H. Tai, Y. Jiang, J. Chen, *Nano Energy* **2021**, *89*, 106321.

[6] a) P. Fathi-Hafshejani, N. Azam, L. Wang, M. A. Kuroda, M. C. Hamilton, S. Hasim, M. Mahjouri-Samani, *ACS Nano* **2021**, *15*, 11461; b) G. Seo, G. Lee, M. J. Kim, S.-H. Baek, M. Choi, K. B. Ku, C.-S. Lee, S. Jun, D. Park, H. G. Kim, S.-J. Kim, J.-O. Lee, B. T. Kim, E. C. Park, S. I.l Kim, *ACS Nano* **2020**, *14*, 5135.

[7] a) A. A. Balandin, *Nat. Mater.* **2011**, *10*, 569; b) P. Rodgers, *Nanoscience and Technology*, World Scientific Publishing, London **2009**.

[8] a) C. Mattevi, H. Kim, M. Chhowalla, *J. Mater. Chem.* **2011**, *21*, 3324; b) X. Li, W. Cai, J. An, S. Kim, J. Nah, D. Yang, R. Piner, A. Velamakanni, I. Jung, E. Tutuc, S. K. Banerjee, L. Colombo, R. S. Ruoff, *Science* **2009**, *324*, 1312.

[9] S. Pezzini, V. Miseiis, S. Pace, F. Rossella, K. Watanabe, T. Taniguchi, C. Coletti, *2D Mater.* **2020**, *7*, 041003.

[10] D. Sarkar, W. Liu, X. Xie, A. C. Anselmo, S. Mitragotri, K. Banerjee, *ACS Nano* **2014**, *8*, 3992.

[11] a) J. L. Hart, K. Hantanasirisakul, A. C. Lang, B. Anasori, D. Pinto, Y. Pivak, J. T. van Omme, S. J. May, Y. Gogotsi, M. L. Taheri, *Nat. Commun.* **2019**, *10*, 522; b) Y. Su, W. Li, X. Cheng, Y. Zhou, S. Yang, X. Zhang, C. Chen, T. Yang, H. Pan, G. Xie, G. Chen, X. Zhao, X. Xiao,

**ADVANCED
SCIENCE NEWS**

www.advancedsciencenews.com

**ADVANCED
MATERIALS
TECHNOLOGIES**

www.advmattechnol.de

B. Li, H. Tai, Y. Jiang, L.-Q. Chen, F. Li, J. Chen, *Nat. Commun.* **2022**, *13*, 4867.

[12] a) L. Wu, X. Lu, Dhanjai, Z.-S. Wu, Y. Dong, X. Wang, S. Zheng, J. Chen, *Biosens. Bioelectron.* **2018**, *107*, 69; b) A. Saleh, S. Wustoni, E. Bihar, J. K. El-Demellawi, Y. Zhang, A. Hama, V. Druet, A. Yudhanto, G. Lubineau, H. N. Alshareef, S. Inal, *J. Phys. Mater.* **2020**, *3*, 044004; c) S. Kumar, Y. Lei, N. H. Alshareef, M. A. Quevedo-Lopez, K. N. Salama, *Biosens. Bioelectron.* **2018**, *121*, 243; d) H. Wang, H. Li, Y. Huang, M. Xiong, F. Wang, C. Li, *Biosens. Bioelectron.* **2019**, *142*, 111531; e) Q. Wei, G. Chen, H. Pan, Z. Ye, C. Au, C. Chn, X. Zhao, Y. Zhou, X. Xiao, H. Tai, Y. Jiang, G. Xie, Y. Su, J. Chen, *Small Methods* **2022**, *6*, 2101051.

[13] X. Zhang, X. Zhao, D. Wu, Y. Jing, Z. Zhou, *Nanoscale* **2015**, *7*, 16020.

[14] M. Quintana, *Biomedical Innovations to Combat COVID-19*, Elsevier, Amsterdam, The Netherlands **2022**.

[15] T. Kim, S. Fan, S. Lee, M.-K. Joo, Y. H. Lee, *Sci. Rep.* **2020**, *10*, 13101.

[16] a) S. Mansouri Majd, A. Salimi, *Anal. Chim. Acta* **2018**, *1000*, 273; b) Y. Yang, X. Yang, X. Zou, S. Wu, D.a Wan, A. Cao, L. Liao, Q. Yuan, X.

Duan, *Adv. Funct. Mater.* **2017**, *27*, 1604096; c) L. Xiang, Z. Wang, Z. Liu, S. E. Weigum, Q. Yu, M. Y. Chen, *IEEE Sens. J.* **2016**, *16*, 8359; d) Y. H. Kwak, D. S. Choi, Y. N. Kim, H. Kim, D. H. Yoon, S.-S. Ahn, J.-W. Yang, W. S. Yang, S. Seo, *Biosens. Bioelectron.* **2012**, *37*, 82; e) O. S. Kwon, S. H. Lee, S. J. Park, J. H. An, H. S. Song, T. Kim, J. H. Oh, J. Bae, H. Yoon, T. H. Park, J. Jang, *Adv. Mater.* **2013**, *25*, 4177.

[17] Y. Sun, G. Niu, W. Ren, J. Zhao, Y. Wang, H. Wu, L. Jiang, L. Dai, Y.-H. Xie, P. Rojo Romeo, J. Bouaziz, B. Vilquin, *AIP Adv.* **2021**, *11*, 065229.

[18] M. Wall, *Therm. Sci.* **2011**, *5*, 1.

[19] J. Ji, L. Zhao, Y. Shen, S. Liu, Y. Zhang, *FlatChem* **2019**, *17*, 100128.

[20] S. K. Vashist, E. Marion Schneider, E. Lam, S. Hrapovic, J. H. T. Luong, *Sci. Rep.* **2014**, *4*, 4407.

[21] a) M. Liu, J. Wu, H. Cheng, *Sci. China Technol. Sci.* **2022**, *65*, 41; b) R. Ye, D. K. James, J. M. Tour, *Acc. Chem. Res.* **2018**, *51*, 1609.

[22] G. Deokar, J. Avila, I. Razado-Colambo, J.-L. Codron, C. Boyaval, E. Galopin, M.-C. Asensio, D. Vignaud, *Carbon* **2015**, *89*, 82.

[23] M. Alhabeb, K. Maleski, B. Anasori, P. Lelyukh, L. Clark, S. Sin, Y. Gogotsi, *Chem. Mater.* **2017**, *29*, 7633.